Aerospace Science and Technology 137 (2023) 108307

Contents lists available at ScienceDirect

Aerospace Science and Technology

journal homepage: www.elsevier.com/locate/aescte

High-fidelity aerodynamic and acoustic design and analysis of a heavy-lift eVTOL

Tao Zhang [a,1], George N. Barakos [a,*], Furqan [b], Malcolm Foster [c]

[a] School of Engineering, University of Glasgow, United Kingdom
[b] Future Flight, GKN Aerospace, United Kingdom
[c] Special Projects, GKN Aerospace, United Kingdom

ARTICLE INFO

Article history:
Received 19 August 2022
Received in revised form 7 February 2023
Accepted 29 March 2023
Available online 3 April 2023
Communicated by Grigorios Dimitriadis

ABSTRACT

This work presents the high-fidelity aerodynamic and acoustic modelling processes supporting the preliminary design of a large eVTOL vehicle at the University of Glasgow in collaboration with GKN Aerospace. To support the GKN heavy-lift eVTOL design, known as Skybus, a range of tools of various fidelity levels were adopted and integrated. This paper first presents the conceptual design and initial sizing of the Skybus vehicle. The airframe design was then analysed using high-fidelity methods with parametric variations of wing an/di-hedral designs. By adjusting the interactions between the wings and the airframe, 5° front wing anhedral combined with 10° aft wing dihedral offered the maximum lift increase. High-fidelity CFD simulations of the complete Skybus vehicle in forward flight with two and four operating propellers were later carried out. The aerodynamic interactions between the propellers and the wings were analysed in detail. In cruise, the four-rotor configuration showed stronger aerodynamic interference effects and hence required more power than the two-rotor counterpart. Near-field acoustics of the vehicle was then extracted directly from the flow solutions and analysed. Far-field noise features were also computed using the FW-H equations and the CFD solutions. The peak noise levels of the heavy-lift vehicle in forward flight at 90 m/s were about 75 dB SPL perceived on the ground 1000 m below. Acoustic features and differences of the two configurations along the flight path and in the lateral directions were presented and discussed.

1. Introduction

Following growing public demands for improved urban transportation, Urban Air Mobility (UAM) concepts have drawn considerable attention from industry and academia in recent years. Thanks to significant advancements in electric propulsion systems, many of the UAM vehicle designs adopted more unconventional configurations for improved performance and reduced carbon/noise emissions. These unconventional configurations often involve multi-rotor systems, convertible designs, and electrical Vertical Taking-Off and Landing (eVTOL) capabilities. Several conceptual designs or prototypes have been unveiled by manufacturers such as Rolls-Royce [1] and Airbus [2]. It is notable, however, that most existing eVTOL designs are aimed at the capacity of 2 to 6 passengers, as an air taxi or a personal vehicle. The possibility of heavy-lift eVTOL vehicles has been rarely explored.

In light of this, GKN Aerospace have proposed the Skybus concept as part of a techno-economic feasibility assessment under the UK ISCF Future Flight Challenge. Skybus aims to take the “Park and Ride” concept into the air, for mass transit over extremely congested routes thus eliminating the 2-dimensional constraints of current surface transport modes including cars, trains, and buses. One application example looks at commuting routes around the London M25 circle into the centre of London within 15 minutes at the maximum capacity of 30 passengers. Compared to the small eVTOL designs, the large size of the Skybus makes it ideal to serve as future aerial public transport, but it poses extra challenges to the vehicle design in terms of the performance, dynamics, and especially the acoustics.

At this preliminary stage, the Skybus concept is designed to be a multi-rotor compound rotorcraft with six wing-tip-mounted, tiltable propellers and three sets of stub lifting surfaces. The initial vehicle sizing and airframe design was completed using simple lifting line and momentum theories. The propellers are envisaged to be powered by electrical motors, thereby having both pitch and

* Corresponding author.
E-mail addresses: t.zhang.4@research.gla.ac.uk, tz77@leicester.ac.uk (T. Zhang), george.barakos@glasgow.ac.uk (G.N. Barakos), furqan@gknaerospace.com (Furqan), Malcolm.Foster@gknaerospace.com (M. Foster).
[1] Currently at the University of Leicester.

https://doi.org/10.1016/j.ast.2023.108307

Nomenclature

Latin

b	Wing Span	m
P	Power	W
p_{ref}	Acoustic Reference Pressure, $p_{ref} = 2 \times 10^{-5}$	[Pa]
$\mathbf{R}$	Residual Vector	
RPM	Revolutions Per Minute	
SPL	Sound Pressure Level, $OSPL = 20log_{10}(\frac{p'}{p_{ref}})$	
T	Thrust	N
$\mathbf{W}$	Conservative Flow Variables	

Subscripts and superscripts

x, y, z	3D Cartesian Directions
i, j, k	3D Block Index

Acronyms

CAD	Computer-Aided Design
CFD	Computational Fluid Dynamics
eVTOL	Electric Vertical Take-off and Landing
FW-H	Ffowcs Williams-Hawkings
HMB3	Helicopter Multi-Block 3
SST	Shear Stress Transport
RANS	Reynolds Averaged Navier Stokes
UAM	Urban Air Mobility

RPM regulations. In hover, or vertical landing/taking-off, all propellers can be tilted vertically to provide thrust countering the vehicle weight and acceleration. The large amount of propellers are intended for this vertical flight mode to carry the weight and to provide redundancy for safety considerations. Wing flaps can also be deployed to reduce the downwash blockage. In forward flight, lift is mainly provided by the wings. The propellers are tilted horizontally to provide thrust countering the overall drag. In forward mode, each propeller is designed be either operating, or stopped and feathered, or folded. The forward flight configuration is not unique due to the redundancy brought by the large number of propellers. The forward flight drag may be easily countered by just one or two sets of the propellers, which are designed to lift the entire vehicle weight in hover. Therefore, this work also presents investigations and comparisons of configuration options in forward flight.

For the design and performance analysis of such unconventional rotorcraft designs, recent studies have highlighted the necessity of high-fidelity modelling methods to resolve the complex flow physics. Recent efforts on the RACER configuration [3–7], which features lateral propellers installed under a lifting main rotor, have reported considerable aerodynamic interactions between the main rotor and the propeller. The rotor/propeller interactions were later specifically investigated through high-fidelity modelling [8,9]. High-fidelity CFD simulations of tilt-rotor aircraft [10,11], winged compound rotorcraft [12], and multi-rotor eVTOL designs [13] have also been reported. These investigations further reported complex aerodynamic interactions among rotors, lifting surfaces, and airframes. Lower-order methods such as lifting lines, blade element theories, and panel methods struggled with such complex aerodynamics and the subsequent acoustic and elastic characteristics. Nonetheless, the high-fidelity CFD modelling is still challenging and difficult due to the complex geometry, numerous moving parts, complicated flow physics, and especially the large computational cost. Advanced techniques e.g. overset/moving/deforming grids, high-order schemes, robust and accurate turbulence modelling are necessary to enable the high-fidelity modelling.

For the present work, the complexity of the Skybus configuration brings additional challenges. This configuration has 6 tiltable propellers and tandem wings. The forward flight mode is of particular interest considering strong interference effects from upstream wings and propellers. It is interesting but challenging to evaluate different propeller arrangements in forward flight and the consequent aerodynamic/acoustic performance changes, and to provide guidance for further development of similar configurations. Another highlight is the large vehicle size and the heavy weight that have been rarely studied, especially in terms of acoustics. As oppose to most investigations focusing on small- to medium-size eVTOL designs [3,12,13], high-fidelity analyses of the heavy-weight Skybus vehicle provide important information to guide future large-size eVTOL designs.

This work presents the high-fidelity aerodynamic and acoustic modelling of the complex Skybus configuration in forward operation using state-of-the-art CFD methods. Accurate and quantitative analyses of the aerodynamic interactions and acoustics provide valuable guidance for the design and operation of heavy-lift eVTOL vehicles. The contents of the present paper are organised as follows: Section 2 presents details of the numerical methods and tools employed for the high-fidelity aerodynamic and acoustic modelling. Section 3 presents discussions of the airframe design with systematic evaluation of the wing anhedral/dihedral angles and corresponding performance changes. Section 4 presents the high-fidelity simulations of the Skybus vehicle in forward flight, with comparisons between different operating configurations. The near-field and far-field acoustic features were also computed and presented. The aerodynamic interactions and acoustic performance were discussed in detail. Section 5 presents the conclusions drawn from the analyses of the Skybus design.

2. Numerical methods and tools

2.1. HMB3 flow solver

As a high-fidelity flow solver and the core of the high-fidelity analysis stage, the in-house Helicopter Multi-Block 3 (HMB3) [14,15] CFD code was used in the present work. The code has been widely used in simulations of rotorcraft flows [9,16–19]. HMB3 solves the Unsteady Reynolds Averaged Navier-Stokes (URANS) equations in integral form using the Arbitrary Lagrangian Eulerian (ALE) formulation for time-dependent domains, which may include moving boundaries. The Navier-Stokes equations are discretized using a cell-centred finite volume approach on a multiblock, structured grid:

$$\frac{d}{dt}\left(\mathbf{W}_{i,j,k}V_{i,j,k}\right) = -\mathbf{R}_{i,j,k}\left(\mathbf{W}_{i,j,k}\right), \quad (1)$$

where i, j, k represent the cell index, $\mathbf{W}$ and $\mathbf{R}$ are the vector of conservative flow variables and residual respectively, and $V_{i,j,k}$ is the volume of the cell i, j, k. To evaluate the convective fluxes, Osher-approximate Riemman solver is used, while the viscous terms are discretized using a second order central difference scheme. The 3^{rd} order MUSCL (Monotone Upstream-centered Schemes for Conservation Laws) approach was used to provide high-order accuracy in space. The chimera/overset grid method [20] was extensively used in this work. In the present work, simulations were performed using the $k-\omega$ SST [21] turbulence model.

2.2. Near-field and far-field acoustic computations

In the present study, the near-field acoustics was directly derived from pressure fields resolved by high-fidelity HMB3 simulations. The sound pressure signals were extracted by subtracting the time-averaged pressure field from raw unsteady data. This direct approach included all acoustic sources in the near-field, subject to the near-field CFD resolution. The similar approach has been used in acoustic analyses of propellers, ducted propellers, and eVTOL vehicles using HMB3 [1,22,23]. This approach requires high-order schemes and fine spatial/temporal resolution. For the current acoustic study, the 3rd-order MUSCL scheme was used.

For simulations of the Skybus vehicle in forward flight, the near-field background grid was carefully tuned to guarantee at least 10 mesh points for the wave length at 10 times the BPF(about 360 Hz), in the 20-metre proximity. Most near-field acoustic evaluations were carried out within 15-metre proximity of the vehicle. The simulations adopted a time step of 1 degree per step of the propeller revolution. This temporal resolution corresponded to at least 60 sampling points for the dominant BPF noise. Smaller steps were desirable but were not used due to high computational costs.

In this work, the far-field acoustics was efficiently calculated using the FW-H equation [24], following the Farassat Formulation 1A [25], taking as input CFD solutions of the surface pressure fields. The formulation has been widely used for far-field noise predictions of aircraft, wind turbines [26], and propellers [23,27,28]. The current far-field acoustic computations were carried out using the in-house acoustic solver HFWH2 (Helicopter Ffows Williams-Hawkings 2), which has been used in previous acoustic computations of propellers and ducted propellers [23,28]. Extensive code-to-code comparisons have also been performed in order to verify the current implementation [27].

The Farassat Formulation 1A [25] solves surface terms of the FW-H equation, i.e. the thickness noise and the loading noise, in the time domain through the introduction of the retarded time concept. The formulation results in two linear equations respectively for the thickness and loading components. The current far-field acoustic approach focused on the non-porous formulation, and ignored the quadrupole source which requires expensive integrations over volumes. In the present work, the Skybus vehicle was designed to have low RPM to reduce noise emissions. The peak tip Mach number encountered throughout this study was about 0.36. The FW-H approach is reasonable considering the subsonic nature of the current study, and is efficient and sufficiently accurate for purposes of initial engineering analyses.

3. Airframe design analysis

The Skybus vehicle is designed with three sets of wings distributed along the fuselage to carry the vehicle weight in forward flight. The wings are all mounted at the top of the fuselage to keep the tip-mounted propeller well away from the ground. An obvious issue of such designs is the aerodynamic interference from upstream wings in forward flight, which has been neglected in the conceptual design stage that employs low-fidelity methods. An effective solution to this issue is to introduce anhedral to the front wing and dihedral to the aft wing, thereby avoiding the direct impingement of upstream wakes.

This section presents the high-fidelity CFD simulations of the airframe design, which systematic variations of the wing anhedral and dihedral angles. The schematic is illustrated in Fig. 1. To minimise the interference, the front wing was given anhedral, and the back wing dihedral, while the middle wing remained unchanged (Fig. 1). The wing anhedral/dihedral angle changes were implemented through an inverse-distance-based mesh deformation module in HMB3 [29].

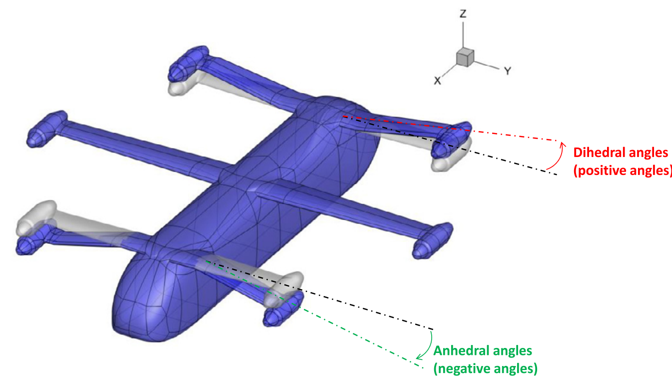

Fig. 1. Schematic of the wing deformation.

HMB3 simulations were performed in forward flight at $AoA = 0°$. In total 10 combinations of the front and back wing deformations were evaluated. The investigated anhedral angles ranged from 0 to 15°, and the dihedral angles ranged from 0 to 10°. Each newly generated configuration with a different anhedral/dihedral angle combinations was denoted by 2 numbers, e.g. $(-5°, 10°)$ represents 5° anhedral to the front wing and 10° dihedral to the back wings.

Flow solutions of configurations $(-5°, 10°)$ and $(-15°, 10°)$ are shown in Figs. 2(a) and 2(b). The anhedral/dihedral angles are clearly effective in alleviating the wake interference. In Fig. 2(a), the wake of the front wing was still partially impinging at the middle wing, while the aft wing effectively avoided the upstream wakes. At the higher front wing angle shown in Fig. 2(b), the wake impingements between wings were completely avoided.

Corresponding overall performance changes brought by the front and aft wing anhedral/dihedral angles, relative to the original configuration, are shown in Figs. 3(a) and 3(b) using Kriging approximations [30]. The response surface was constructed using 10 sample points shown in the figures using '+', including the original configuration. We used the Ordinary Kriging model with a constant regression and a Gaussian correlation function [31]. The approximation parameters were solved using the Maximum Likelihood estimation [31]. The response surface construction was verified using the Leave-One-Out (LOO) strategy, and the standard deviation of the relative prediction errors at each sampling point is 1.17% for the lift and 2.69% for the drag, respectively.

In Figs. 3(a) and 3(b), the overall lift and drag changes brought by the an/dihedral angles were complex with local minima and maxima. The performance changes generally were more sensitive to the anhedral angles of the front wing, which is expected, considering its upstream position. The introduction of an/di-hedral angles resulted in overall lift increases compared to the original design. A local maximum lift increase of about 4 kN can be observed at $(-5°, 9°)$. The minimal lift increase of 0.5 kN was observed near $(-15°, 5°)$. In terms of drag, however, the an/dihedral angles resulted in both increases and decreases. Drag reductions were mostly associated with low anhedral angles of the front wing. A maximum drag reduction of about 0.7 kN was observed near $(-2.5°, 7.5°)$. As the front wing anhedral angle was increased, the overall drag increased. The maximum drag increase was about 1.1 kN for the $(-15°, 7.5°)$ configuration.

To further analyse the an/di-hedral impact, Figs. 4(a) to 5(d) present the lift and drag changes of each airframe component, i.e. fuselage, front, middle, and aft wings. Figs. 4(a) to 4(d) show clearly that major lift increases originate from the middle wing and especially the aft wing. The aft wing lift was increased by 2 to 3 kN as the anhedral/dihedral angles were increased. This was expected as both changes would free the aft wing from upstream wakes as shown in Figs. 2(a) and 2(b). The fuselage and front wing

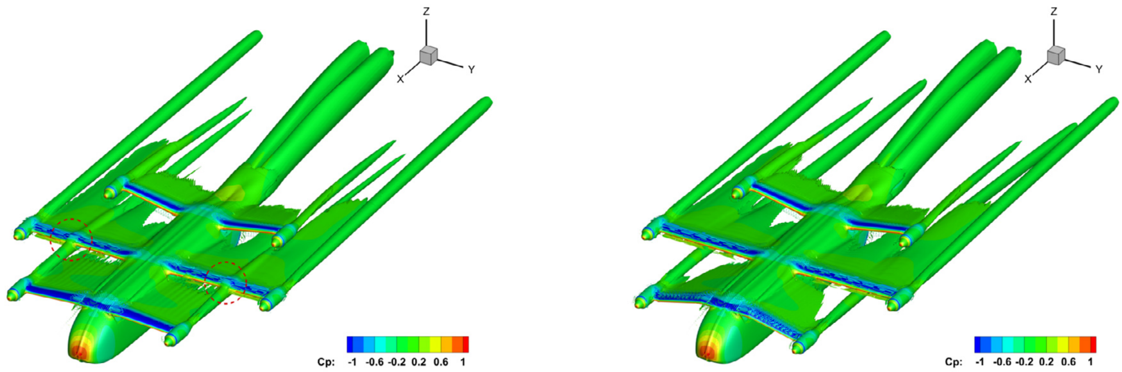

(a) Configuration (−5°, 10°)

(b) Configuration (−15°, 10°)).

Fig. 2. Flow solutions of different anhedral/dihedral combinations visualised using iso-surfaces of dimensionless Q criterion = 1, coloured with pressure coefficients. (For interpretation of the colours in the figure(s), the reader is referred to the web version of this article.)

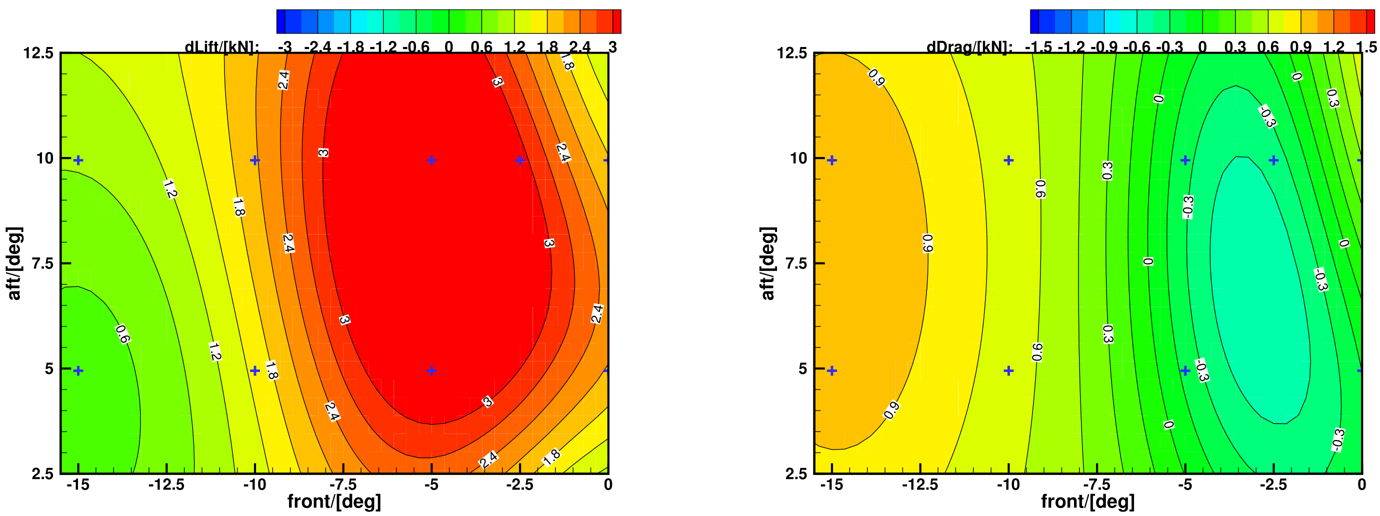

(a) Lift changes.

(b) Drag changes.

Fig. 3. Overall lift and drag changes relative to the initial configuration due to the anhedral/dihedral angle changes of the front and back wings ("+" denotes the sample points).

lift changes, as shown in Figs. 4(a) and 4(b), were dominated by the front wing anhedral angles. They produced decreased lift as the anhedral increased. This was mostly due to the interference between the front wing and the fuselage, as indicated by the front wing loading shown in Fig. 4(b). The wing root sectional lift was significantly decreased as anhedral increased.

For the middle wing, the lift increase was mostly dominated by the front wing anhedral. A maximum increase of about 1.5 kN was observed at −7.5° anhedral. Further increasing or decreasing the anhedral would reduce the lift benefit. This is further investigated in Fig. 6(b) by extracting the middle wing loading distribution along the span. As shown in Fig. 6(b), for the initial configuration ((0°, 0°)), there was considerably increased lift from 65% span to the wing tip. This was caused by the front wing tip vortex impingement as shown in Fig. 2(a). Due to the vortex rotational direction, the outer part of the wing had increased lift due to the increased induced AoA, while the inner section saw decreased lift. The overall lift change depends on the strength of these two effects, and these can be adjusted by the upstream wing anhedral angle. As shown in Fig. 6(b), as the upstream anhedral angle was increased, this interaction was first strengthened then gradually weakened. According to the lift changes in Fig. 4(c), this interaction led to the peak benefit at the −7.5° anhedral angle.

Figs. 5(a) to 5(d) present the component drag changes. Note that the fuselage (Fig. 5(a)) was the major drag contributor and the drag changes closely followed the anhedral changes. Large anhedral angles led to increased drag due to wing-fuselage interference. The front and middle wing drag changes largely followed their lift changes. For the aft wing, however, its drag was reduced while its lift was increased. The aft wing drag loading distribution along the wing span was hence extracted and presented in Fig. 6(c). As can be noted, the initial configuration had high drag near the aft wing tip, which was caused by upstream tip vortex impingement. As the anhedral/dihedral angles were increased, the aft wing was freed from the wake interference. Although the inner sections had slightly increased drag, the overall drag was still reduced thanks to the elimination of the strong interference.

Performance changes brought by the wing deformations were complex and non-linear due to aerodynamic interference between wings and the fuselage. The current results suggest that a low anhedral angle for the front wing accompanied by a moderate dihedral angle to the aft wing would be beneficial in terms of both lift increase and drag reduction. To maximise the lift gain, later design analysis focused on configuration (−5°, 10°), which was the closest to the optimal lift gain among all samples.

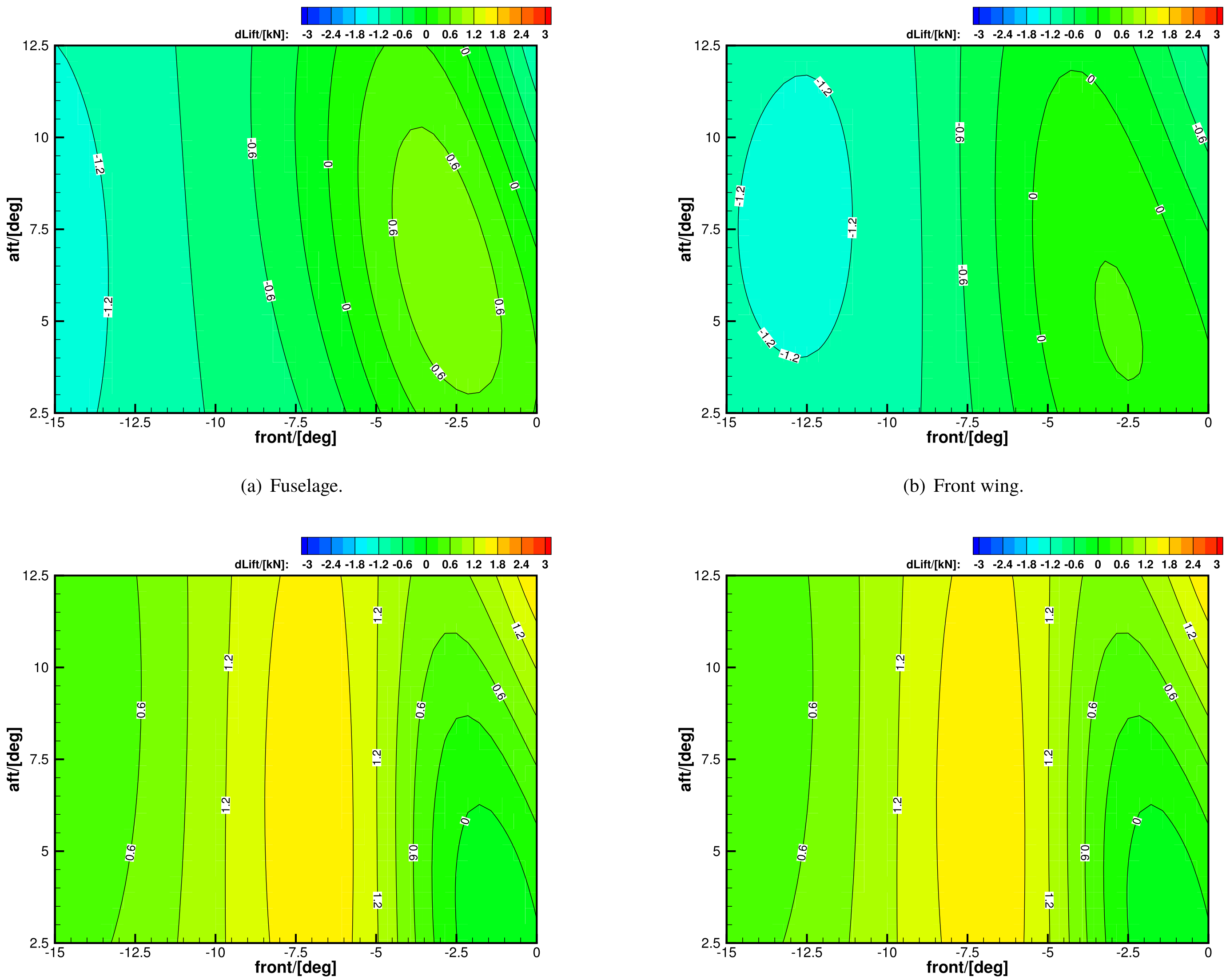

(a) Fuselage.

(b) Front wing.

(c) Middle wing.

(d) Aft wing.

Fig. 4. Component lift changes relative to the initial configuration due to the anhedral/dihedral angle changes of the front and back wings.

4. Aerodynamic/acoustic evaluations of Skybus in forward flight

This section presents the high-fidelity aerodynamic and acoustic simulations of the Skybus vehicle in forward flight. As mentioned earlier, the Skybus vehicle is a six-rotor, heavy-lift eVTOL design. Due to the large number of propellers, plenty of control and operating redundancy can be expected. The current design allows each of the six rotors to be either folded, stopped and feathered, or producing thrust at a certain pitch/RPM setting. As shown in Fig. 7, several configurations are available for forward flight.

The simplest and cleanest configuration, in terms of aerodynamic interference, is the two-rotor configuration with four propellers folded (hence excluded from the modelling). While the six-rotor configuration, i.e. all propellers rotating and producing thrust, is the most complex configuration with the highest aerodynamic interference. Assuming the same phase and rotation directions for all rotors, any performance output of the Skybus vehicle in forward flight, either aerodynamic or acoustic, would depend on the combinations of the pitch/RPM settings of each propellers. This function is expected to be highly non-linear and complex, and certain pitch/RPM settings would surely deliver the optimum aerodynamic or acoustic performance. To explore the aerodynamic/acoustic performance of the vehicle in forward flight, high-fidelity numerical methods are necessary considering the complex aerodynamic interference between rotors, lifting surfaces, and the airframe, yet the computational cost of assessing the complete function space through high-fidelity methods would be prohibitively high. This section presents high-fidelity HMB3 simulations of the simplest two-rotor configuration with all other rotors folded, as well as, a four-rotor configurations with the aft propellers stopped and feathered.

4.1. HMB3 simulations of the two-rotor and four-rotor configurations

The two-rotor configuration in forward flight refers to the configuration where only the two middle-wing propellers are operating, and all other rotors are assumed folded and therefore excluded from modelling, as shown in Fig. 8(a). The four-rotor configuration in this work, shown in Fig. 8(b), refers to the configuration where the front and middle propellers are operating, while the aft propellers are stopped and feathered. Table 1 presents the vehicle design characteristics and operating conditions for the forward flight simulations. Note that the two- and four-rotor configurations

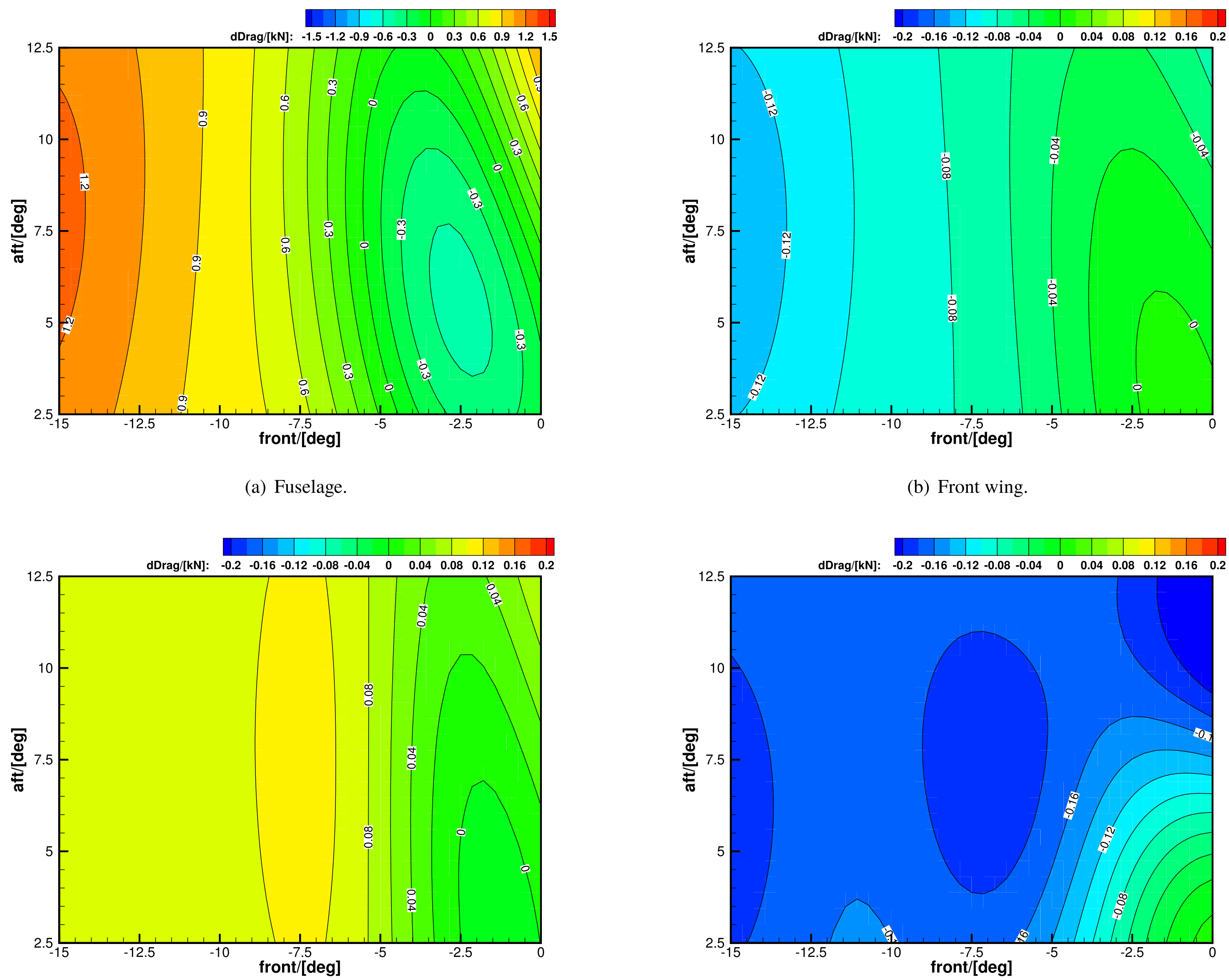

(a) Fuselage.

(b) Front wing.

(c) Middle wing.

(d) Aft wing.

Fig. 5. Component drag changes relative to the initial configuration due to the anhedral/dihedral angle changes of the front and back wings.

Table 1
Operating conditions of the Skybus forward flight simulations (the blade design details can be found in Ref [32]).

	Two-rotor	Four-rotor
Altitude	1000 m	
Forward flight speed	90 m/s	
Operational weight	117 kN	
Vehicle incidence	0°	1°
Vehicle side-slip	0°	
Operating propellers	2	4
Propeller tip Mach	0.34	
Blade number	6	
Propeller radius	3.25 m	
Propeller rotation	top-in (counter rotating)	

had the same weight, because the front/aft rotors were assumed folded in the two-rotor configuration but were excluded from the simulations for simplicity. All propellers are six-bladed and of the same blade design. More details of the blade design including the design process can be found in Ref. [32]. Note that each set of the propellers could operate at different RPM/pitch setting subject to the trimming results as shown in Table 3. All propellers were counter rotating in a top-in manner for acoustic benefits [22], so the rolling moment was balanced.

High-fidelity HMB3 simulations of the Skybus vehicle were carried out with the help of overset grids. The grid topology for the four-rotor configuration is presented in Fig. 9. Grids for different components were generated separately, with the help of the employed automatic grid generation [33,34], and assembled later using chimera methods for the CFD computation. The simulations adopted the URANS formulation with the k-ω SST turbulence model. The third-order MUSCL scheme was used to improve the spatial resolution. A symmetry plane was used as shown in Fig. 9 to halve the computational domain and reduce the computational cost.

Details of the grid sizes for the two- and four-rotor configurations are presented in Table 2. The mesh size and spacing adopted recommendations from previous high-fidelity simulations of unconventional rotorcraft configurations [3,7,12]. The propeller blades were assigned 2.2 million cells each. The near-body grid enclosing the propellers had a spacing ranging from 0.035 to 0.15 of the blade 75% chord length. The first layer height of the grids near wall

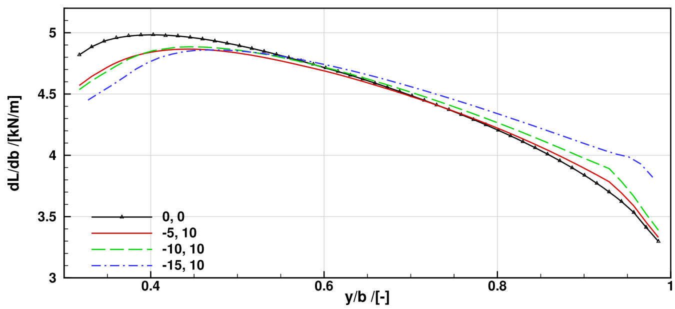

(a) Front wing lift loading.

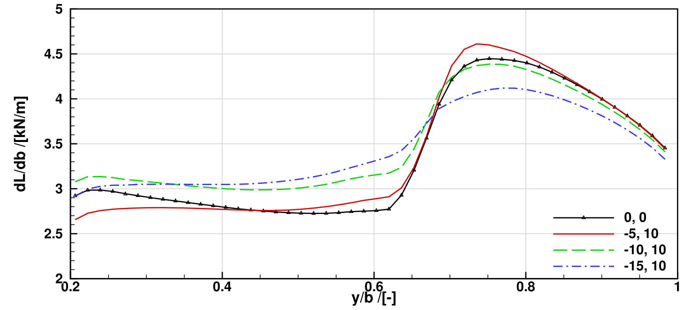

(b) Middle wing lift loading.

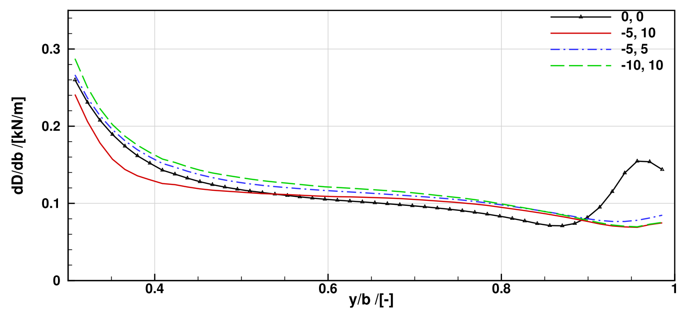

(c) Aft wing drag loading.

Fig. 6. Wing loading changes due to anhedral/dihedral variations.

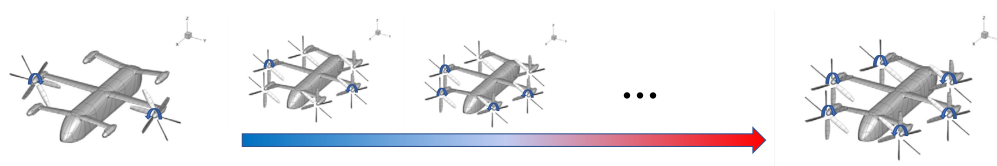

Fig. 7. Configuration options for the Skybus in forward flight.

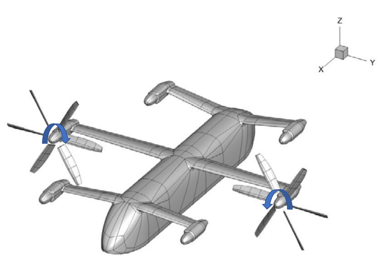

(a) Two-rotor configuration.

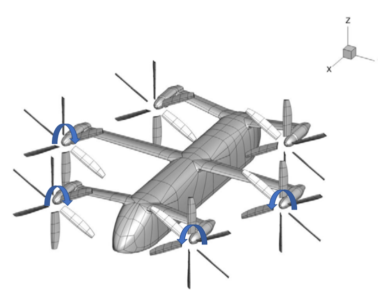

(b) Four-rotor configuration.

Fig. 8. The two-rotor and four-rotor configuration of the Skybus vehicle for operations in forward flight.

Table 2
Grid details of HMB3 simulations of the two- and four-rotor configurations in forward flight for the half model (in million cells).

Configurations	Blades	Airframe	Local refinement	Background	Total
two-rotor	2.2×6	20.7	12.8	0.8	47.6
four-rotor	2.2×18	25.3	15.7	0.8	81.4

surfaces was carefully adjusted to keep the y+ value near 1. The off-body local refinement grid had a spacing of 0.15 of the blade chord, within 4 to 5 radii away from the vehicle. This also ensured at least 10 points for the acoustic wave length at 10 times the BPF as mentioned earlier. In total, about 81 million cells were used for the half-model of the four-rotor configuration. For simulations of the two-rotor configuration, a similar grid topology and simulation strategy was used, but the overall cell number was reduced to about 47 million thanks to the removal of the front/aft propeller blades and their associated local refinement grids. A time step of $1^\circ/step$ was adopted, as suggested by previous temporal resolution studies [7], and considering the dominant axial flight features of the current work.

In the present work, the trimming of the vehicle in forward flight was accomplished by making initial estimations using the high-fidelity performance evaluations of the isolated airframe and propellers, then gradually altering the propeller pitch angles and the vehicle AoA as the simulation progresses. The clean airframe

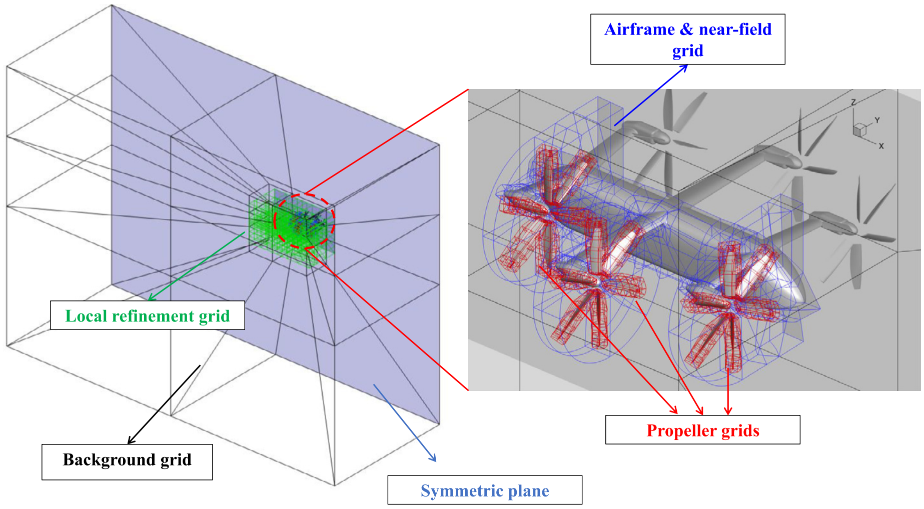

Fig. 9. Grid details and overset topology for simulations of the Skybus in forward flight.

Table 3
Propeller operating conditions of the two- and four-rotor configurations. The 2-element tuples (β, RPM) represent the propeller pitch/RPM combinations.

Configuration	Front propeller	Middle propeller	Aft propeller
two-rotor	– (folded)	$(45.3^\circ, 356)$	– (folded)
four-rotor	$(45.8^\circ, 340)$	$(46.8^\circ, 340)$	$(90^\circ, 0)$ (feathered)

performance was first evaluated using high-fidelity simulations as has been presented in previous sections. The propeller performance was also evaluated using HMB3 at various pitch/RPM combinations and performance maps [32] were constructed to interpolate for operating conditions. The trimming target in the present work is to meet a target lift while having zero net drag, by adjusting the propeller RPM and collective pitch, and the vehicle pitch angle. The yawing and rolling moments were balanced because the port- and starboard-side rotors were counter-rotating (symmetry). The pitching moment was not included as the vehicle centre of gravity was not known yet. The vehicle was assumed in forward flight at 90 m/s. The clean airframe lift at $AoA = 0^\circ$ was chosen as the target lift, which corresponded to about 85% of the vehicle Maximum Take-off Weight. Propeller RPM/pitch settings were initially interpolated from the performance maps [32] to counter the overall vehicle drag with the least power.

Of course, such propeller performance estimations ignored installation effects, aerodynamic interactions, and hence further adjustments were expected as the high-fidelity simulations progress. Initially, it was assumed that all propellers produce the same thrust at the same RPM and pitch settings, but the pitch settings were later modified as the simulations progressed. The final propeller operating conditions are shown in Table 3. It should be highlighted that, for the two-rotor case, no correction to the operating condition was needed at all. This suggested that aerodynamic interactions in this case were not significant. For the four-rotor case, as the high-fidelity simulations evolved, the middle propeller was producing considerably lower thrust, and the overall drag was higher than expected, so its collective pitch was increased by 1° as shown in Table 3. A considerable lack of lift was noticed in this case, hence the vehicle AoA was adjusted to 1° to boost the lift generation. This lack of lift was due to the aft wing suffering from the aerodynamic interactions, and is discussed below.

Figs. 10(a) and 10(b) present the trimming residuals. The overall lift and drag values were normalised by the corresponding clean airframe lift L_0 and drag D_0 at $AoA = 0^\circ$. Both configurations fulfilled the lift requirement. The two-rotor configuration countered the overall drag with a negligible thrust redundancy of about 0.03 D_0 (about 0.3 kN). The four-rotor case, however, had a larger difference of about 0.13 D_0 (about 1 kN) net drag. This was due to the strong aerodynamic interactions, as well as, the increased drag due to the 1° attitude.

Table 4 presents the drag contributions from each component for the 2-rotor and 4-rotor configurations, as well as for the clean airframe. All drag values were normalised by the clean airframe drag D_0 at $AoA = 0^\circ$ to highlight the drag changes. As can be noted, the 2-rotor configuration differed only slightly from the clean airframe. As for the four-rotor case, the feathered aft propellers produced a significant drag contribution of 0.59 D_0 and was the major source of drag second only to the middle wing. This contributed to the 0.13 D_0 net drag and later studies hence attempted to adjust the feathering angle to eliminate the drag.

Fig. 11 presents the aft propeller drag changes at different feathering angles. The drag values were normalised by the D_0 value. It can be noted that the minimum drag of about 0.5 D_0 can be obtained when the blade pitch was set at 85°. However, this was still a considerable amount of drag. Further decreasing or increasing the feather angle would lead to significantly increased drag. The drag force may be further reduced by e.g. folding the blades but this may not be technically possible for the actual aircraft.

4.2. Aerodynamic performance and interactions

Flow features of the two-rotor and four-rotor configurations resolved by the HMB3 simulations are presented in Figs. 12(a) and 12(b). For the two-rotor configuration in Fig. 12(a), the flow-filed was dominated by the clearly-resolved wakes of the two propellers, as well as, their interactions with downstream wings and nacelles. For the four-rotor configuration in Fig. 12(b), however, the flow features were much more complex. The wakes of the front propellers impinged partially on the middle-wing propellers. The wakes of the front and middle propellers then joined together to attack the downstream wings the aft propellers. The stopped and feathered aft propellers managed to slightly reduce the complex, swirling flow. Still, strong and complex wakes were tailed behind the vehicle.

To analyse the rotor-to-wing interference, Figs. 13(a) to 13(c) present the time-averaged wing lift loading distributions along the wing span for two-/four-rotor configurations and the correspond-

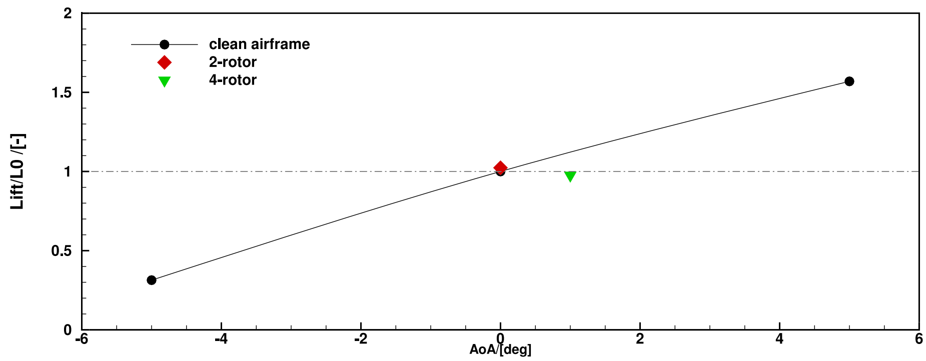

(a) Lift.

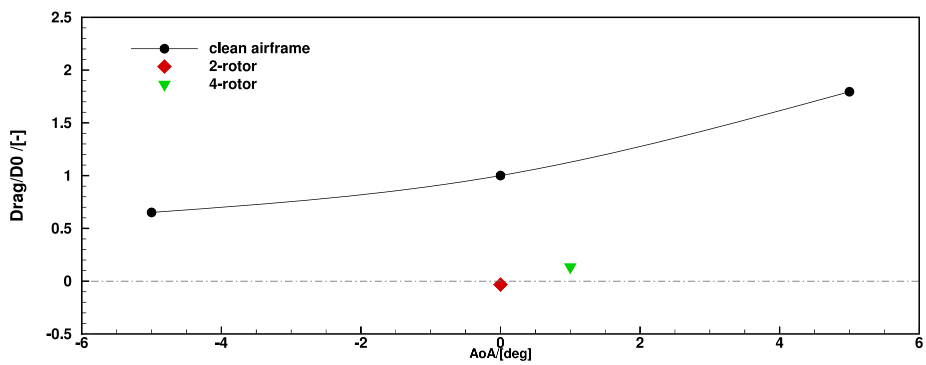

(b) Drag.

Fig. 10. Vehicle trimming results for the 2- and 4-rotor configurations.

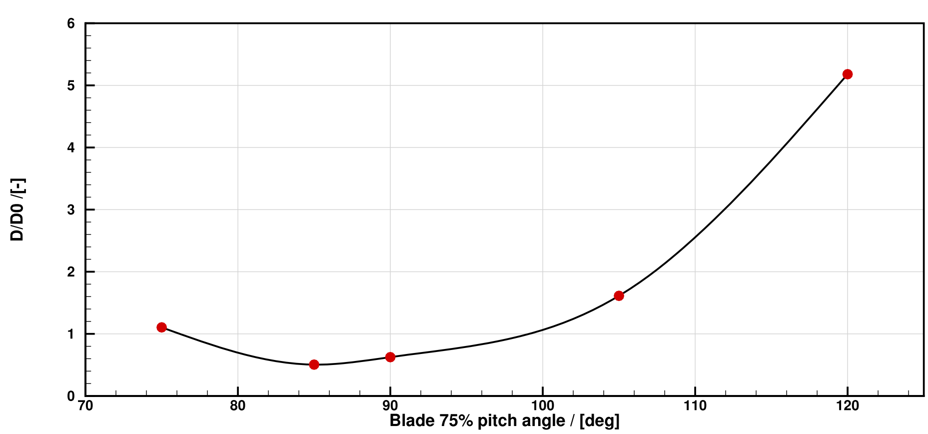

Fig. 11. Aft propeller drag variations of the four-rotor configuration at different feathering angles.

Table 4
Breakdown of drag contributions in forward flight. All component drag forces were normalised by the total drag D0 of the clean airframe at $AoA = 0°$ (first row). Negative values denote thrust forces.

Configuration	Airframe				Propellers			Sum
	Fuselage	Front wing	Middle wing	Aft wing	Front	Middle	Aft	
clean airframe ($AoA = 0°$)	0.33	0.09	0.36	0.21	–	–	–	1.00
2-rotor ($AoA = 0°$)	0.34	0.10	0.39	0.22	–	-1.10	–	-0.04
clean airframe ($AoA = 1°$)	0.34	0.12	0.41	0.24	–	–	–	1.11
4-rotor ($AoA = 1°$)	0.36	0.17	0.52	0.21	-0.73	-0.97	0.59	0.13

ing clean airframes. For the two-rotor configuration at $AoA = 0°$, the front and aft wings experienced negligible changes, as shown in Figs. 13(a) and 13(c), respectively. The middle wing (Fig. 13(b)) showed larger changes, mostly lift reductions from 60% span to the tip. The tip-mounted propellers weakened the beneficial effects brought by the upstream wing tip vortices. This was expected as the propellers were rotating top-in, hence the induced velocity should reduce the effective AoA for the outer sections of the wing. The inner sections were not affected since the rotor wake could not reach as shown in Fig. 12(a).

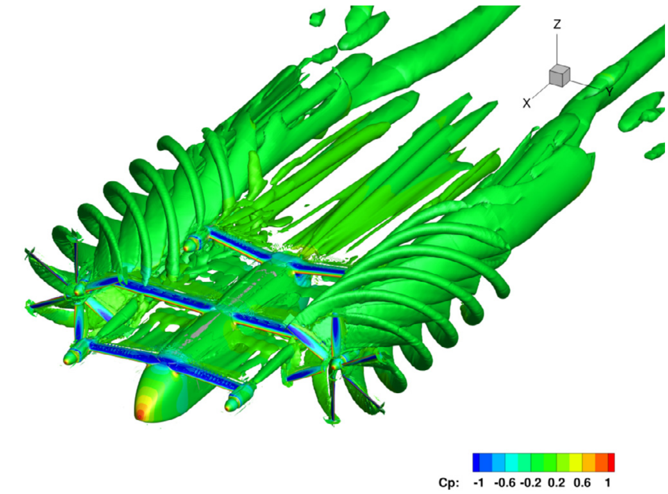

(a) Two-rotor configuration.

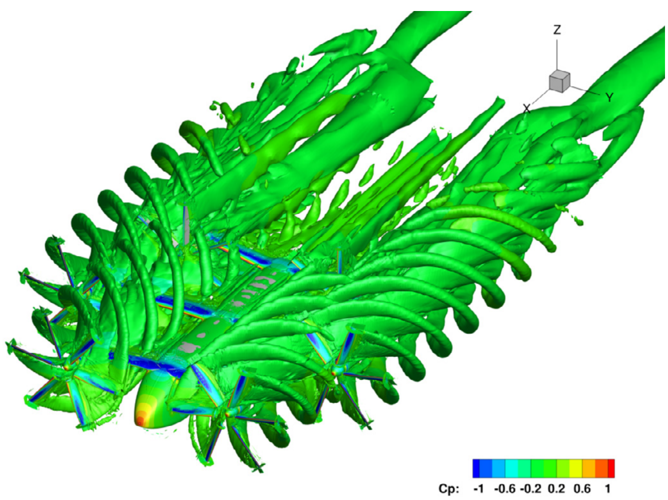

(b) Four-rotor configuration.

Fig. 12. Instantaneous Q-criterion iso-surfaces of the two-rotor and four-rotor configurations in forward flight, coloured using pressure coefficient values.

As for the four-rotor configuration, the strong aerodynamic interactions affected the wings. As shown in Fig. 13(a), the front wing lift loading was reduced along its span until about 85%. This was consistent with Fig. 12(b) considering that the front wing was completely immersed in the propeller wake. The small increase near the wing tip could be associated with interactions with the nacelle and blade root. The middle wing (Fig. 13(b)) also experienced considerable interactions. The wing tip sections showed lift decreases similar to the two-rotor case, while the wing root sections also showed some lift decreases associated with the upstream propeller wakes. In Fig. 13(c), the aft wing experienced the most severe lift losses. Due to upstream wakes from the front and middle propellers, the aft wing was unable to produce any lift and was indeed producing downwards forces. These explained the lack of lift as noted in the description of the trimming process.

To analyse the wing-to-rotor interference, the propeller disk loading changes with respect to the corresponding isolated cases are presented in Figs. 14(a) to 14(c). The wireframes represent the corresponding front or middle wings. For these wing-tip-mounted propellers, the interference effects were mostly limited in regions overlapping with the wings. The wing interference results in thrust increases in these regions, especially near the blade tip. This was primarily caused by the effective up-wash due to the wing thickness and blockage [11]. For the two-rotor configuration in Fig. 14(a), the interference region extended $\pm 30°$ of azimuth angles ahead and after blade passage near the wing. For the four-rotor front propeller (14(b)), the interference region increased to about $\pm 60°$ of azimuth, suggesting stronger interference effects since the propeller RPM and thrust were lower. As for the four-rotor middle propeller (Fig. 14(c)), in addition to the wing interference, some interference was also noted on the left side of the propeller disk, which corresponds to the upstream propeller wake impingement as shown in Fig. 12(b).

Table 5
Propeller and vehicle performance comparisons between the two-rotor and four-rotor configurations. All data here was normalised using the propeller performance of the two-rotor configuration (T_0, P_0), where T_0 stands for the propeller thrust and P_0 denotes the propeller power.

Configuration	Propeller			Total Power
	Front	Middle	Aft	
Two-rotor	–	(T_0, P_0)	–	$2P_0$
Four-rotor	$(0.66T_0, 0.78P_0)$	$(0.88T_0, 0.92P_0)$	–	$3.4P_0$

Table 5 compares the propeller and vehicle performance between the two- and four-rotor configurations. Note that all performance data was normalised by the propeller performance of the two-rotor configuration (T_0, Q_0) to highlight performance changes. Here, T_0 stands for the propeller thrust and Q_0 denotes the propeller power. Compared to the middle propeller of two-rotor configuration, the front and middle propellers of the four-rotor configuration individually produced lower thrust and required lower power. The middle propellers carried slightly higher thrust than the front propellers due to their higher pitch angle. However, the overall vehicle power of the current four-rotor configuration, i.e. the propeller power values combined, were $1.4P_0$ higher than that of the two-rotor configuration.

Overall, the two-rotor configuration showed only mild aerodynamic interference. The rotor-to-wing interference was limited within the propeller radius and was negligible elsewhere. The wing-to-rotor interference was limited near the rotor tip regions overlapping with the wing. The four-rotor configuration had stronger interference effects due to excessive upstream rotor wakes. The wake impingement caused wing lift losses. Particularly, the aft wing was not producing any lift due to the strong upstream wakes. The feathered aft propellers contributed about 30% of the overall drag, and the front and middle propellers had to produce more thrust at higher power. The front propeller wake was ingested by the downstream middle propeller, and the middle propeller's power consumption had to be further increased and its disk loading was disturbed. As a combined result, the four-rotor configuration required 1.7 times the power of the two-rotor configuration in forward flight.

4.3. Near-field acoustics

This section presents the near- and far-field acoustic features derived from the high-fidelity HMB3 solutions of the Skybus vehicle in forward flight, along with comparisons of the two- and four-rotor configurations. The near-field acoustics was directly extracted from the flow solution, while the far-field acoustics was computed using the HFWH2 code following the non-porous Farassat Formulation 1A, using the HMB3 surface pressure solutions as input.

First, the near-field acoustic analyses focused on the airframe surfaces to identify the noise sources. Fig. 15(a) presents the instantaneous surface sound pressure values on the airframe of the two-rotor configurations in forward flight. Fig. 15(b) presents the corresponding Root-Mean-Square (RMS) values of the surface acoustic signals and reflects the strength of the surface loading noise sources. The rotating blades were represented by wireframes

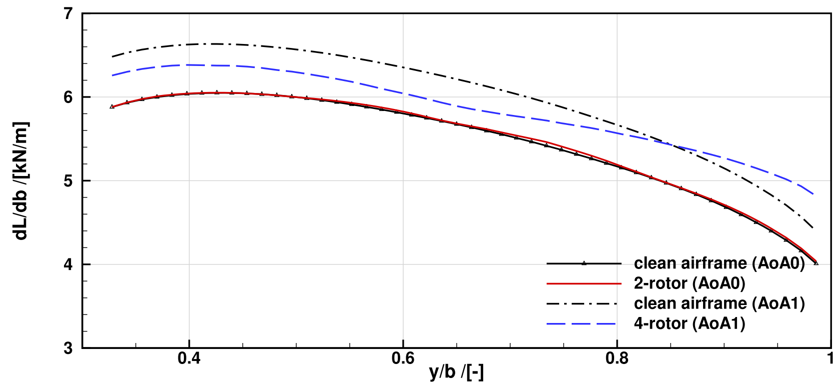

(a) Front wing.

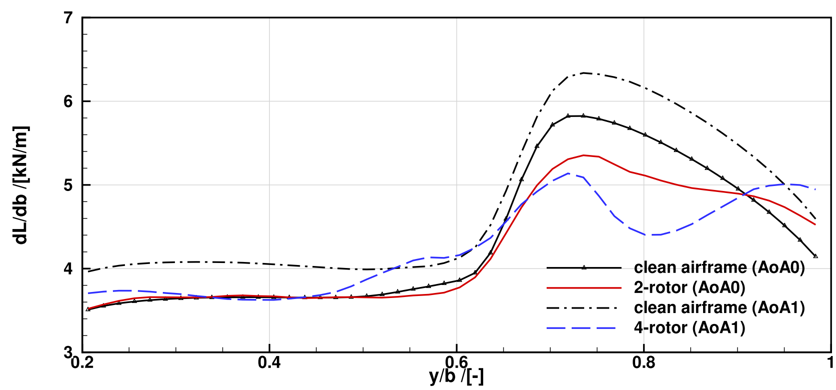

(b) Middle wing.

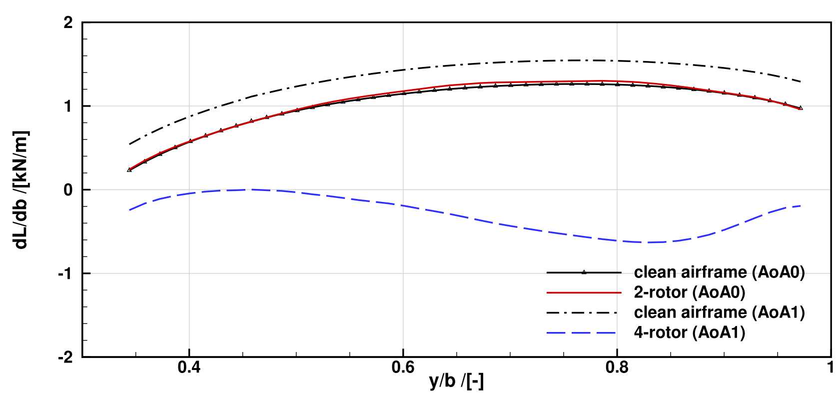

(c) Aft wing.

Fig. 13. Wing lift loading changes due to propeller interference.

to bring out features on the airframes. In Figs. 15(a) and 15(b), few loading noise sources on the airframe can be easily identified, i.e. outboard regions of the middle wing and the downstream nacelles. Correlating with the flow solutions of Fig. 12(a), these regions coincided with the propeller wake impingement on the airframe, and were mostly due to aerodynamic interference. The fuselage and the upstream wing showed minor pressure fluctuations.

Figs. 16(a) and 16(b) present the instantaneous sound pressure contours on the airframe of the four-rotor configuration in forward flight, and the corresponding RMS values. The operating front and middle propellers are also represented by wireframes. Compared to the two-rotor case, stronger surface pressure fluctuations were observed all over the airframe surface. The main noise sources on the airframe were the front wings, the middle wings and nacelles, the aft wings and nacelles, and the stopped aft propeller blades. These regions also coincided with the propeller wakes of Fig. 12(b), suggesting that these were also mainly results of aerodynamic interference.

Figs. 17(a) and 17(d) present the acoustic Sound Pressure Levels (SPL) on a 15-metre-radius sphere enclosing the entire Skybus vehicle for the two- and four-rotor configurations, respectively. The SPL values were computed directly from sound pressure signals extracted from the HMB3 simulations.

In Fig. 17(a), for the two-rotor configuration, strong noise was perceived downstream the vehicle. This is consistent with the flow details of Fig. 12(a). Another region of high noise was seen around

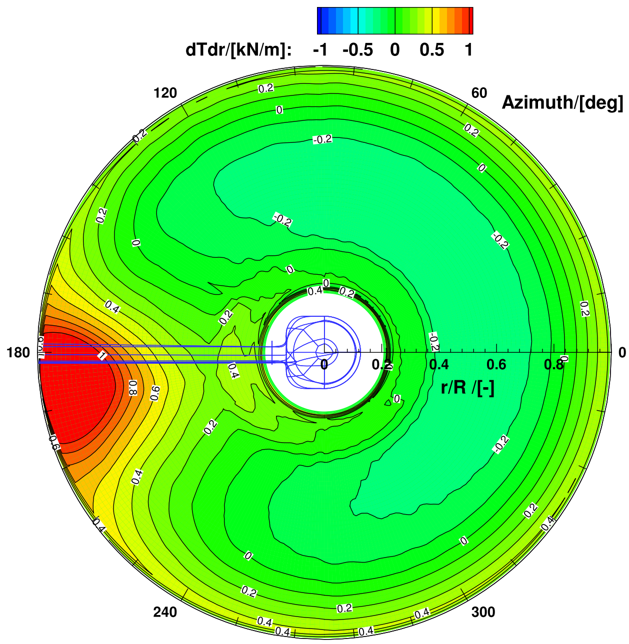

(a) Two-rotor configuration middle propeller disk.

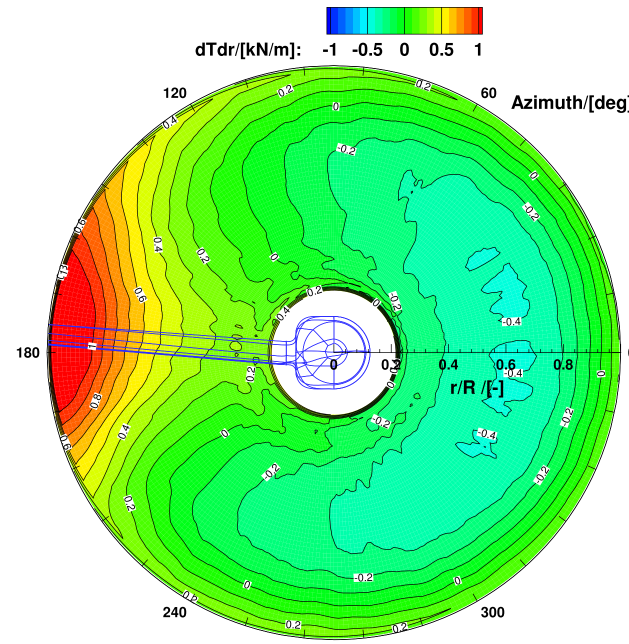

(b) Four-rotor configuration front propeller disk.

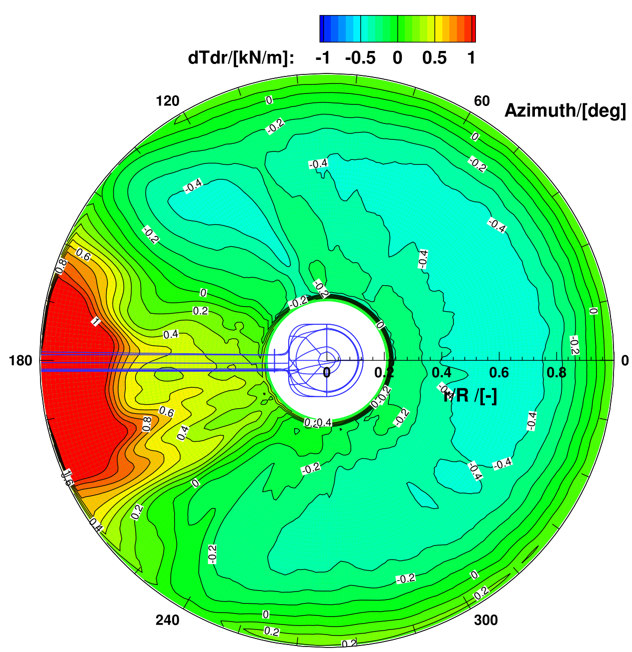

(c) Four-rotor configuration middle propeller disk.

Fig. 14. Propeller disk loading changes due to aerodynamic interference (viewed from the trailing edge of the wing). The wireframes represent the corresponding front and middle wings.

the front of the vehicle (Fig. 17(b)), on both starboard and port sides. This is associated with the noise directivity of the propellers. The near-field acoustic pattern of this two-rotor configuration suggests that the vehicle is likely to produce strong noise when approaching and leaving.

In Fig. 17(c), for the four-rotor configuration, it can be noticed that the levels were higher than that for the two-rotor case, and the acoustic directivity was considerably different. The acoustic levels of the four-rotor configuration were 5 to 10 dB higher than the two-rotor case, in all directions. In terms of directivity, high noise levels were also perceived in the vehicle wake, which correlates well with the flow features shown in Fig. 12(b). Strong noise was also perceived near the middle propellers in the lateral directions and below the vehicle as shown in Fig. 17(d).

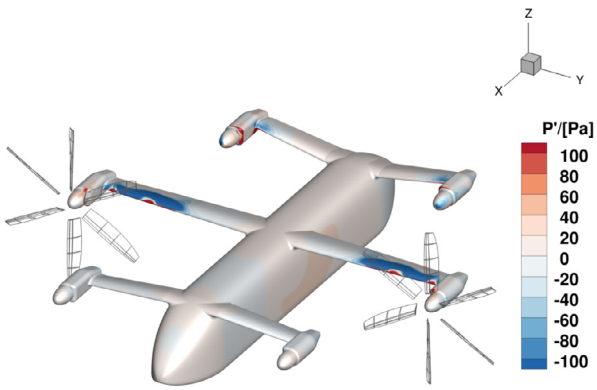

(a) Instantaneous surface sound pressure contours.

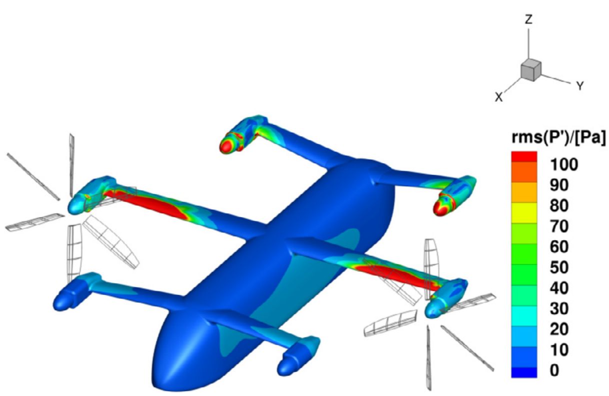

(b) Root-Mean-Square (RMS) values of the surface sound pressure contours.

Fig. 15. Surface sound pressure contours and fluctuation levels on the airframe of the two-rotor configuration in forward flight. Moving blades are presented by wire-frames.

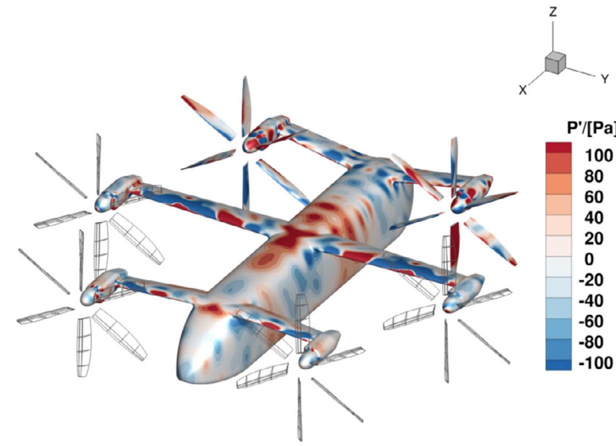

(a) Instantaneous surface sound pressure contours.

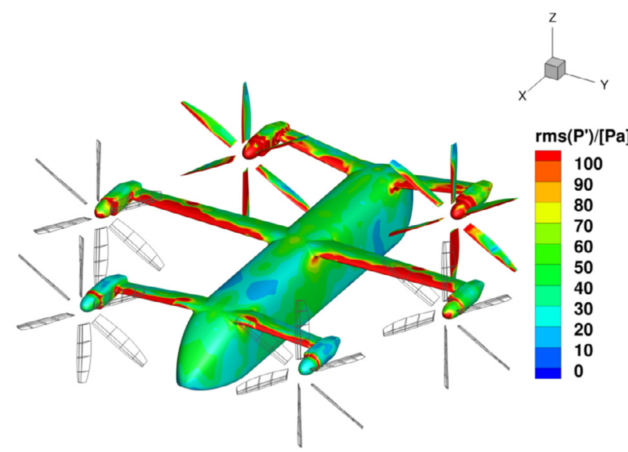

(b) Root-Mean-Square (RMS) values of the surface sound pressure contours.

Fig. 16. Surface sound pressure contours and fluctuation levels on the airframe of the four-rotor configuration in forward flight. Moving blades are presented by wire-frames.

4.4. Far-field acoustics

Far-field acoustics of the two- and four-rotor configurations in forward flight were also computed. The acoustic propagation used the in-house HFWH2 code following the non-porous Farassat formulation 1A [25]. The far-field acoustic results only contain the thickness and loading components. The unsteady, high-fidelity HMB3 flow solutions of the Skybus, along with the fully-resolved blade motions, were used as input panels into the HFWH2 code.

Figs. 18(a) and 18(b) present the ground noise projection 1000 metres below the vehicle for the two- and four-rotor configurations. The X axis represents the vehicle flight path, in level flight along the +X direction. The vehicle is set at the origin (0 m, 0 m) as denoted by the dash-dot lines. The +Y axis represents the port-side direction. The starboard side was not shown as the simulation was fully symmetric with counter-rotating blades on port/starboard sides.

In Fig. 18(a), it can be seen that the far-field acoustics of the two-rotor configuration, showed strong directivities towards the downstream and lateral directions. Along the vehicle longitudinal direction (X axis), the noise gradually increased when approaching. A maximum noise level of about 72 dB was perceived about 400 metres behind the vehicle. The noise level gradually reduced to about 60 dB at 2500 metres. Along the lateral direction, the noise decayed quickly to about 60 dB beyond 1000 metres. A low noise region can be noted covering the area ($X < -1200$ m, $Y > 700$ m) with noise levels around 55 dB. These far-field noise features are consistent with the near-field solutions of Fig. 17(a), as high near-field noise levels were observed near the vehicle nose and downstream.

Compared to the two-rotor configuration, the acoustic features of the four-rotor configuration, as shown in Fig. 18(b), were considerably different. In the longitudinal direction, the vehicle noise gradually increased when approaching and led to a maximum level of 78 dB after the vehicle passage. The noise level decayed faster downstream compared to that of the two-rotor configuration. The noise level decayed to 56 dB, 2500 metres after the vehicle passage ($X < -2500$ m). Along the lateral direction, for regions -1000 m $< X <$ 1000 m, the noise decreased to about 68 dB beyond 1500 metres. The noise, however, decayed little along the lateral direction for regions with $X < -1000$ m.

Fig. 19 compares the acoustic features of the two- and four-rotor configurations along the flight path, i.e. the X axes in Figs. 18(a) and 18(b). In Fig. 19, both configurations showed similar acoustic features along the flight path, i.e. gradually increasing noise when approaching, maximum noise levels near the vehi-

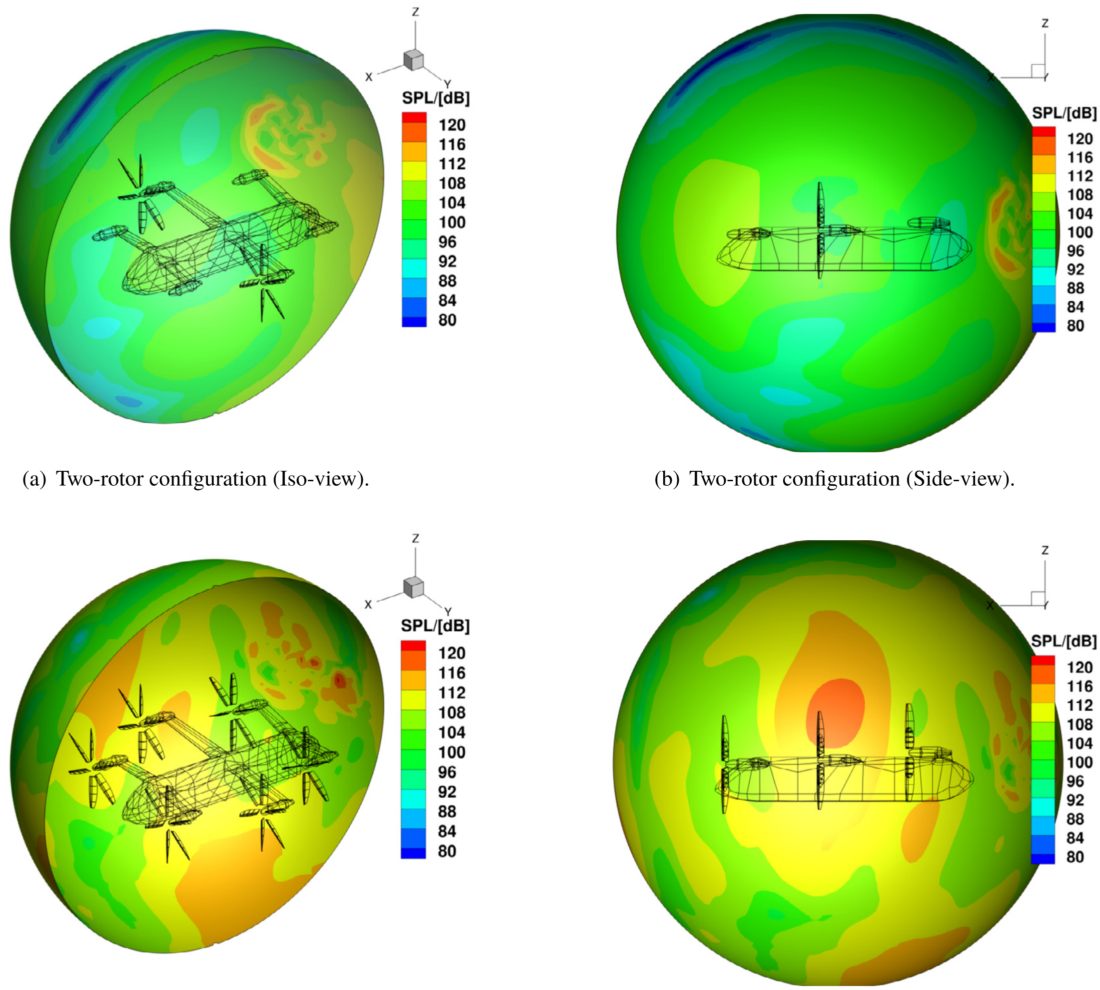

(a) Two-rotor configuration (Iso-view).

(b) Two-rotor configuration (Side-view).

(c) Four-rotor configuration (Iso-view).

(d) Four-rotor configuration (Side-view).

Fig. 17. SPL contours on a 15-metre-radius sphere enclosing the vehicle.

cle passage, and gradually reduced noise when moving away. The maximum noise levels were about 72 dB and 78 dB for the two- and four-rotor configurations, respectively. The four-rotor configuration showed consistently stronger noise than that of the two-rotor configuration when $X > -1000$ m. It is interesting to notice that the noise level of the four-rotor configuration became lower for $X < -1000$ m. This further reflected the differences in the noise directivities of the two configurations, as the four-rotor configuration projected more noise towards the lateral direction. These features are also consistent with the near-field acoustics of Fig. 17(c).

5. Conclusions

This work presented the initial numerical design and analysis of the heavy-lift Skybus eVTOL concerning aerodynamics and acoustics. The wing anhedral/dihedral design was parametrically analysed using high-fidelity CFD simulations and Kriging approximations. The complete Skybus vehicle in forward flight was then simulated, and two configurations were investigated. The following conclusions can be drawn from the present investigation:

1) Significant aerodynamic interference was observed due to the wakes of upstream wings. The upstream front wing tip vortex induced increased lift on the outer sections of the middle wing, and reduced lift on the inner section. By introducing anhedral to the front wing and dihedral to the aft wing, the interference strength was adjusted. The upstream wing wake also caused increased drag near the aft wing tip. Complex effects of the wing an/di-hedral were visualised and analysed systematically with the help of Kriging models. A 5-degree anhedral angle to the front wing and a 10-degree dihedral angle to the aft wing were selected to maximise the lift gain while maintaining drag reductions.
2) High-fidelity HMB3 simulations of the complete Skybus vehicle including the designed propellers in forward flight were also carried out. Two configurations with different numbers of operating propellers, i.e. the two- and four-rotor configurations, were investigated. The wing loading changes and propeller disk loading changes were extracted to quantify the aerodynamic interference. For the studied operating conditions, the four-rotor configuration showed stronger aerodynamic interference due to upstream propeller wakes. The feathered aft propeller, contributed considerable drag, and the aft wing was unable to provide lift due to the interference. The front propeller wake also affected the middle propeller disk loading. The total power required by the four-rotor configuration was about 1.7 times that of the two-rotor configuration.
3) In terms of acoustic features, both configurations projected noise of 70 to 75 dB to the ground in forward flight. The four-rotor configuration showed stronger noise due to aerodynamic interactions. The noise directivities of the two con-

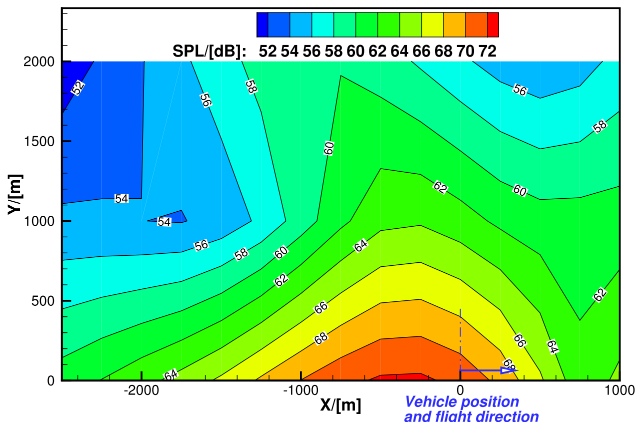

(a) Two-rotor configuration.

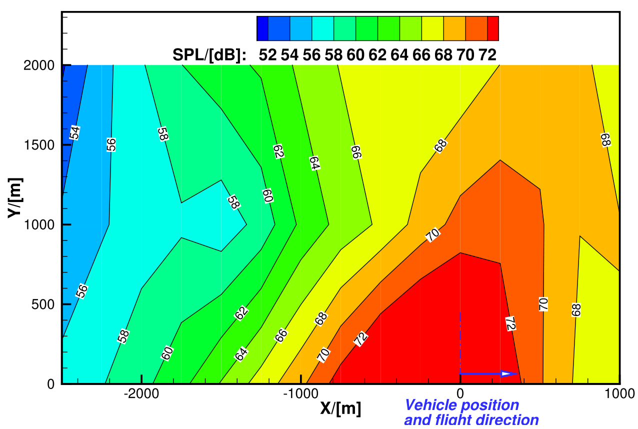

(b) Four-rotor configuration.

Fig. 18. Far-field acoustic contours of the vehicle perceived 1000 metres below the vehicle.

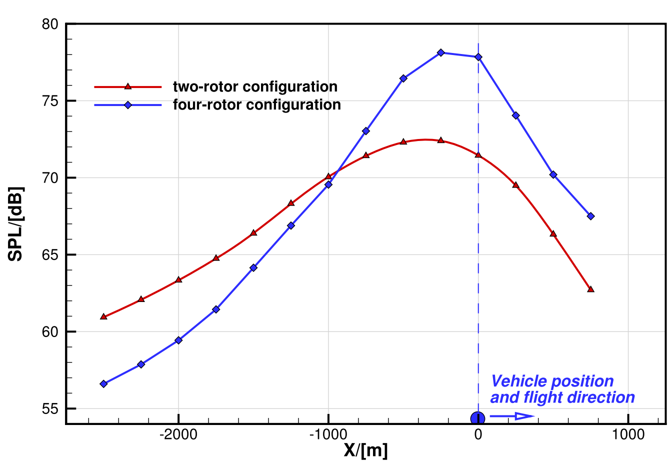

Fig. 19. Acoustic levels of the two-rotor and four-rotor configurations along the flight path 1000 metres below.

figurations were also different. The four-rotor configuration showed strong directivity towards the lateral directions, while the two-rotor configuration projected the noise mostly along the longitudinal direction. Along the flight path, the four-rotor configuration showed about 5 dB higher noise when approaching, but the noise quickly reduced and became identical to that of the two-rotor configuration at 1000 metres after the vehicle passage. After 1000 metres, the four-rotor configuration became quieter, and the noise reduction reached a maximum of about 4 dB at 2500 metres.

Future design and analysis work on the Skybus concept will continue and more high-fidelity aerodynamic/acoustic analyses of the vehicle at various conditions will be delivered, aiming to refine the initial design.

Declaration of competing interest

The authors declare that they have no known competing financial interests or personal relationships that could have appeared to influence the work reported in this paper.

Data availability

The authors do not have permission to share data.

Acknowledgement

The authors would like to acknowledge GKN Aerospace for their support and approval of publication.

References

[1] R. Higgins, G. Barakos, S. Shahpar, I. Tristanto, A computational fluid dynamic acoustic investigation of a tiltwing eVTOL concept aircraft, Aerosp. Sci. Technol. 111 (2021) 106571, https://doi.org/10.1016/j.ast.2021.106571.

[2] L. Arlen, H. Gemmink, CityAirbus, a safe entry into remote piloted flight test world, in: 47th European Rotorcraft Forum (Virtual), 2021.

[3] F. Frey, J. Thiemeier, C. Öhrle, M. Keßler, E. Krämer, Aerodynamic interactions on Airbus Helicopters' compound helicopter RACER in cruise flight, J. Am. Helicopter Soc. 65 (4) (2020) 1–14, https://doi.org/10.4050/JAHS.65.042001.

[4] F. Frey, C. Öhrle, J. Thiemeier, M. Keßler, E. Krämer, Aerodynamic interactions on Airbus Helicopters' compound helicopter RACER in hover, in: Vertical Flight Society 76th Annual Forum, 2020.

[5] C. Öhrle, U. Schaferlein, M. Keßler, E. Krämer, Higher-order simulations of a compound helicopter using adaptive mesh refinement, in: The AHS International 74th Annual Forum & Technology Display, Phoenix, Arizona, USA, 2018.

[6] C. Öhrle, F. Frey, J. Thiemeier, M. Kebler, E. Krämer, Coupled and trimmed aerodynamic and aeroacoustic simulations for Airbus Helicopters' compound helicopter RACER, J. Am. Helicopter Soc. 64 (2019) 1–14, https://doi.org/10.4050/JAHS.64.032003.

[7] J. Thiemeier, C. Öhrle, F. Frey, M. Keßler, E. Krämer, Aerodynamics and flight mechanics analysis of Airbus Helicopters' compound helicopter RACER in hover under crosswind conditions, CEAS Aeronaut. J. 11 (1) (2020) 49–66, https://doi.org/10.1007/s13272-019-00392-3.

[8] R. Boisard, L. Lefevre, T. Zhang, G. Barakos, A. Visingardi, F. Lößle, A. Kostek, T. Andronikos, M. Keßler, R. Wickersheim, A. Colli, G. Gibertini, A. Zanotti, Rotor/rotor aerodynamic interactions–a Garteur action group, in: 33rd Conference of the International Council of the Aerospace Sciences, ICAS22, Stockholm, Sweden, 4–6 September, 2022.

[9] T. Zhang, G.N. Barakos, High-fidelity numerical investigations of rotor-propeller aerodynamic interactions, Aerosp. Sci. Technol. 124 (2022) 107517.

[10] J. Lim, S. Tran, Interactional structural loads of the XV-15 rotor in airplane mode, in: Proceedings of the 45th European Rotorcraft Forum, Warsaw, Poland, 2019, pp. 17–20.

[11] J. Lim, Fundamental investigation of proprotor and wing interactions in tiltrotor aircraft, in: The VFS 75th Annual Forum & Technology Display, Philadelphia, Pennsylvania, the USA, 2021.

[12] H. Sugawara, Y. Tanabe, Numerical investigation of rotor/wing aerodynamic interactions at high advance ratios, J. Aircr. 56 (6) (2019) 2285–2298, https://doi.org/10.2514/1.C035370.

[13] S. Miesner, M. Keßler, E. Kramer, Interactional structural loads of the XV-15 rotor in airplane mode, in: The Vertical Flight Society's 77th Annual Forum And Technology Display, Virtual, May 10–14, 2021.

[14] R. Steijl, G.N. Barakos, K. Badcock, A framework for CFD analysis of helicopter rotors in hover and forward flight, Int. J. Numer. Methods Fluids 51 (8) (2006) 819–847, https://doi.org/10.1002/fld.1086.

[15] M. Biava, M. Woodgate, G.N. Barakos, Fully implicit discrete-adjoint methods for rotorcraft applications, AIAA J. 54 (2) (2015) 735–749, https://doi.org/10.2514/1.J054006.

[16] A. Antoniadis, D. Drikakis, B. Zhong, G. Barakos, R. Steijl, M. Biava, L. Vigevano, A. Brocklehurst, O. Boelens, M. Dietz, et al., Assessment of CFD methods against experimental flow measurements for helicopter flows, Aerosp. Sci. Technol. 19 (1) (2012) 86–100, https://doi.org/10.1016/j.ast.2011.09.003.
[17] R. Steijl, G. Barakos, CFD analysis of complete helicopter configurations–lessons learnt from the GOAHEAD project, Aerosp. Sci. Technol. 19 (1) (2012) 58–71, https://doi.org/10.1016/j.ast.2011.01.007.
[18] A.J. Garcia, G.N. Barakos, Numerical simulations on the ERICA tiltrotor, Aerosp. Sci. Technol. 64 (2017) 171–191, https://doi.org/10.1016/j.ast.2017.01.023.
[19] T. Zhang, G.N. Barakos, Toward vehicle-level optimization of compound rotorcraft aerodynamics, AIAA J. 60 (3) (2022) 1937–1957.
[20] M. Jarkowski, M. Woodgate, G. Barakos, J. Rokicki, Towards consistent hybrid overset mesh methods for rotorcraft CFD, Int. J. Numer. Methods Fluids 74 (8) (2014) 543–576, https://doi.org/10.1002/fld.3861.
[21] F. Menter, Two-equation eddy-viscosity turbulence models for engineering applications, AIAA J. 32 (8) (1993) 1598–1605, https://doi.org/10.2514/3.12149.
[22] G. Chirico, G.N. Barakos, N. Bown, Propeller installation effects on turboprop aircraft acoustics, J. Sound Vib. 424 (2018) 238–262.
[23] T. Zhang, G.N. Barakos, High-fidelity numerical analysis and optimisation of ducted propeller aerodynamics and acoustics, Aerosp. Sci. Technol. 113 (2021) 106708, https://doi.org/10.1016/j.ast.2021.106708.
[24] J.E. Ffowcs Williams, D.L. Hawkings, Sound generation by turbulence and surfaces in arbitrary motion, Philos. Trans. R. Soc. Lond. Ser. A, Math. Phys. Sci. 264 (1151) (1969) 321–342.
[25] F. Farassat, Derivation of formulations 1 and 1A of Farassat, Tech. rep., NASA/TM-2007-214853, 2007.
[26] V.V. Dighe, F. Avallone, G. van Bussel, Effects of yawed inflow on the aerodynamic and aeroacoustic performance of ducted wind turbines, J. Wind Eng. Ind. Aerodyn. 201 (2020) 104174, https://doi.org/10.1016/j.jweia.2020.104174.
[27] D.A. Smith, A. Filippone, G.N. Barakos, Acoustic analysis of counter-rotating open rotors with a locked blade row, AIAA J. (2020) (available online), https://doi.org/10.2514/1.J059273.
[28] T. Zhang, G. Qiao, D. Smith, G. Barakos, A. Kusyumov, Parametric study of aerodynamic performance of equivalent ducted/un-ducted rotors, Aerosp. Sci. Technol. 117 (2021) 106984, https://doi.org/10.1016/j.ast.2021.106984.
[29] M. Biava, G.N. Barakos, Optimisation of ducted propellers for hybrid air vehicles using high-fidelity CFD, Aeronaut. J. 120 (1232) (2016) 1632–1657, https://doi.org/10.1017/aer.2016.78.
[30] J. Sacks, S.B. Schiller, W.J. Welch, Designs for computer experiments, Technometrics 31 (1) (1989) 41–47, https://doi.org/10.1080/00401706.1989.10488474.
[31] J. Martins, A. Ning, Engineering Design Optimization, 2021.
[32] T. Zhang, G. Barakos, M. Foster, et al., Multi-fidelity aerodynamic design and analysis of propellers for a heavy-lift eVTOL, Aerosp. Sci. Technol. 135 (108185) (2023), https://doi.org/10.1016/j.ast.2023.108185.
[33] T. Zhang, G.N. Barakos, High-fidelity CFD validation and assessment of ducted propellers for aircraft propulsion, J. Am. Helicopter Soc. 66 (1) (2021) 1–28, https://doi.org/10.4050/JAHS.66.012008.
[34] T. Zhang, G.N. Barakos, Development of simulation tools for high fidelity analysis of compound rotorcraft, in: AIAA Scitech 2020 Forum, 2020, p. 1258.